Electronic Supplementary Material (ESI) for Catalysis Science & Technology.

Enhanced activity of H_2O_2-treated copper(II) oxide nanostructures for the electrochemical evolution of oxygen

Albertus D. Handoko, Suzi Deng, Yilin Deng, Andy Wing Fai Cheng, Kuang Wen Chan, Hui Ru Tan, Yanlin Pan, Eng Soon Tok, Chorng Haur Sow and Boon Siang Yeo

Supplementary Information

1. Characterisation of Cu_2O nanostructure precursors and H_2O_2-treated CuO nanostructures

1.1. Scanning electron microscopy of Cu_2O nanostructures

Nanostructured Cu_2O precursors consist of nanowire networks that extend into the micrometres regime (Fig S1a). Transmission electron microscopy (TEM) images indicate that the networks were formed by interpenetrating/branching growth of individual nanowires 50-100 nm in diameters (Fig S1b). The nanostructures were verified by selected area electron diffraction (SAED) to be single-crystalline Cu_2O (insets of Fig S1b). Analysis of the *d*-spacings in the high resolution TEM (HRTEM) images showed well-resolved (0 0 1) lattice planes of Cu_2O (Fig S1c).

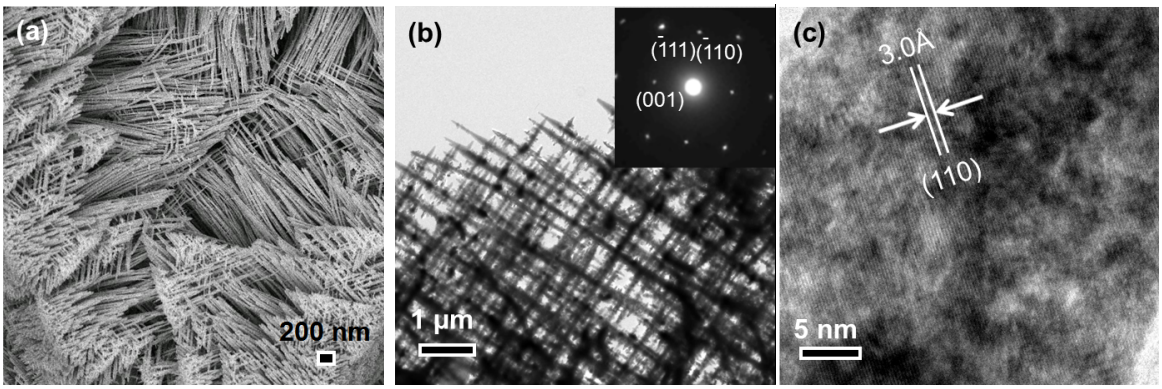

Figure S1: (a) Scanning and (b-c) transmission electron microscopy images of Cu_2O nanostructures at different magnifications. Selected area electron diffraction pattern shown in the inset in (b) and d-spacing analysis in the high resolution image (c) confirms the chemical identity of the precursor as Cu_2O.

1.2. Quantitative XRD analysis of various Cu_2O and CuO powders used in this work.

To obtain lattice parameter data using the Bruker Topas 4.2 platform, X-ray diffraction data was treated with whole pattern decomposition analysis as described by Pawley[1] and Toraya[2] . Only the most robust parameters such as lattice parameters, angles and crystallite size were refined. The crystallite size reported here refers to the volume-weighted mean crystallite size, extracted from the integral breadth of each line profile. Zero error and instrumental broadening of the diffractometer were considered. The literature was consulted to obtain reference cell data of Cu_2O,[3] CuO,[4] Cu.[5] The refinement results for the various Cu_2O and CuO powder samples are presented in sections 1.2.1. to 1.2.3. The blue, red and grey lines represent observed XRD data, calculated pattern from the reference data, and difference plot respectively.

1.2.1. Cu_2O nanostructures

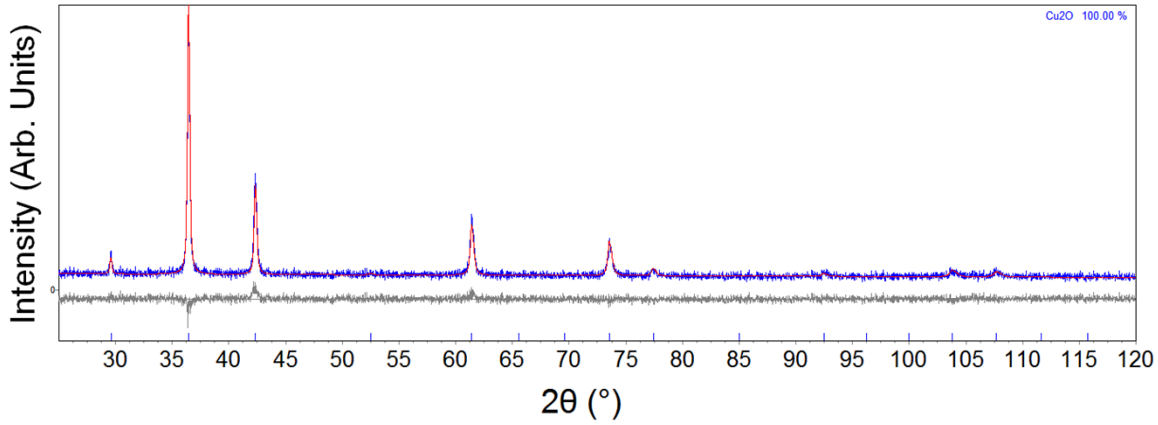

Figure S2: X-ray diffraction data of Cu_2O nanostructures after whole powder pattern decomposition fitting.

Table S1: Whole pattern decomposition fitting results for Cu_2O nanostructures.

Phase Name	**Cu_2O (100%)**	
R-Bragg	4.113	
Space group	Pn-3m	
Cell Volume	77.854(45)	($Å^3$)
Crystallite size (Lvol-IB)	27.67(86)	(nm)
Crystal Linear Absorption Coefficient	288.97(17)	(1/cm)
Crystal Density	6.1040(35)	(g/cm^3)
Lattice Parameters	a 4.26999(82)	(Å)

1.2.2. H_2O_2-treated CuO nanostructures

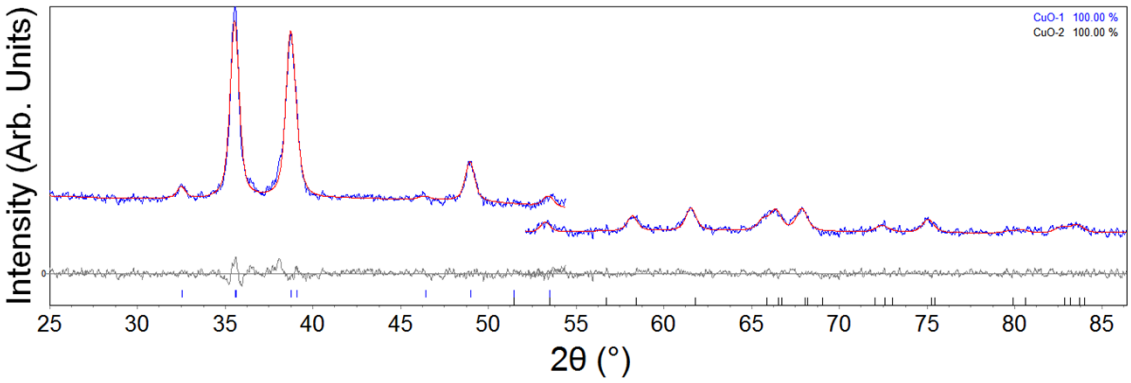

Figure S3: X-ray diffraction data of H_2O_2-treated CuO nanostructures after whole powder pattern decomposition fitting. The diffraction data was collected with Bruker Discover D8 with GADDS area detector at two different detector positions, resulting in different background intensity levels.

Table S2: Whole pattern decomposition fitting results for H_2O_2-treated CuO nanostructures.

Phase Name	**CuO (100%)**		
R-Bragg	0.799		
Space group	C1c1		
Cell Volume	81.208(30)		(Å^3)
Crystallite size (Lvol-IB)	12.61(11)		(nm)
Crystal Linear Absorption Coefficient	284.55(11)		(1/cm)
Crystal Density	6.5062(24)		(g/cm^3)
Lattice Parameters	a	4.67548(53)	(Å)
	b	3.43263(78)	(Å)
	c	5.1275(15)	(Å)
	β	99.3141(97)	°

1.2.3. Commercial Cu_2O (Alfa Aesar)

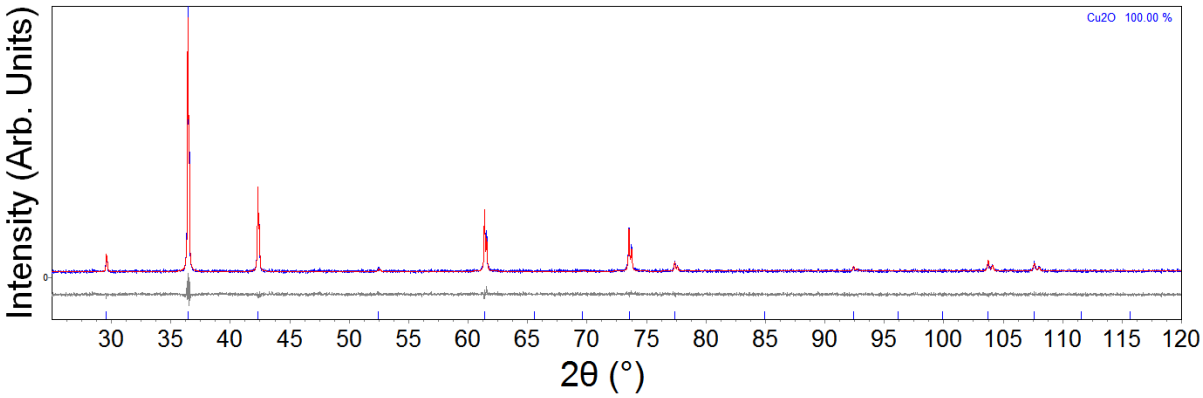

Figure S4: X-ray diffraction data of untreated commercial Cu_2O after whole powder pattern decomposition fitting.

Table S3: Whole pattern decomposition fitting results for untreated commercial Cu_2O.

Phase Name	**Cu_2O (100%)**	
R-Bragg	2.254	
Space group	Pn-3m	
Cell Volume	77.8151(43)	($Å^3$)
Crystallite size (Lvol-IB)	162.3(31)	(nm)
Crystal Linear Absorption Coefficient	289.113(16)	(1/cm)
Crystal Density	6.10704(33)	(g/cm^3)
Lattice Parameters	a 4.269280(78)	(Å)

1.3. Cu 2*p* XPS signal of as-grown Cu_2O nanostructures and H_2O_2-treated CuO nanostructures

X-ray photoelectron spectroscopy (Fig S5) confirms that the as-synthesised nanostructures were Cu_2O. These were oxidised to CuO after H_2O_2 treatment.[6, 7]

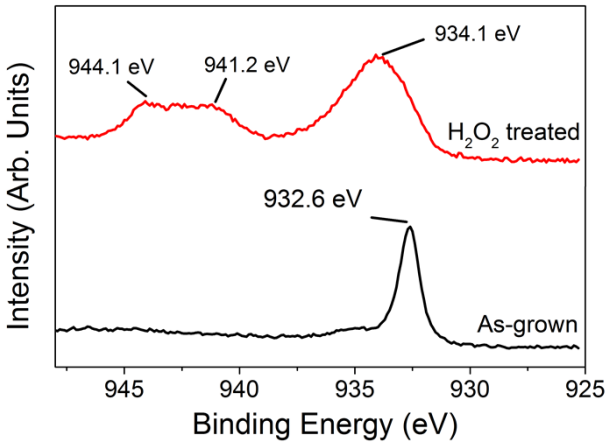

Figure S5: XPS spectra for Cu_2O nanostructures (black trace) and H_2O_2-treated CuO nanostructures (red trace). The satellite shakeup peaks between 941 to 945 eV belonging to CuO can only be observed on the H_2O_2-treated CuO nanostructures.

2. Scanning electron microscopy of Cu_2O nanostructures exposed to heat treatment at 400 °C for 1 hour

Cu_2O nanostructures that have been heat treated at 400°C in air for 1 hr oxidised to 200-300 nm sized CuO cuboids (Figure S6a-b).

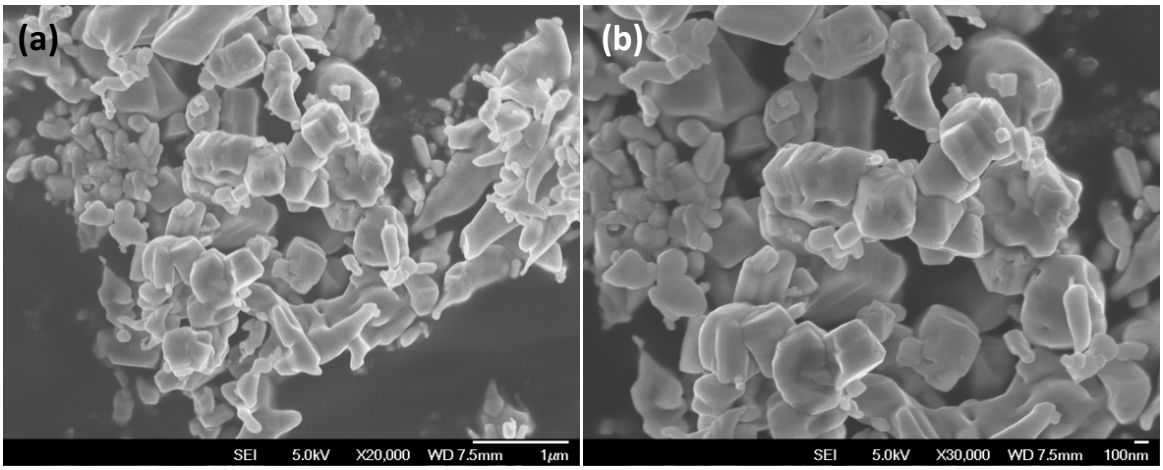

Figure S6: (a and b) Cu_2O nanostructures after heat treatment at 400 °C for 1 hour.

A quantitative analysis of the XRD data of heat treated Cu_2O nanostructures was performed (Figure S7 and Table S4). Only CuO phase was detected. The literature was consulted to obtained reference cell data for CuO.[4] The blue, red and grey lines represent observed XRD data, calculated pattern from the reference data, and difference plot respectively.

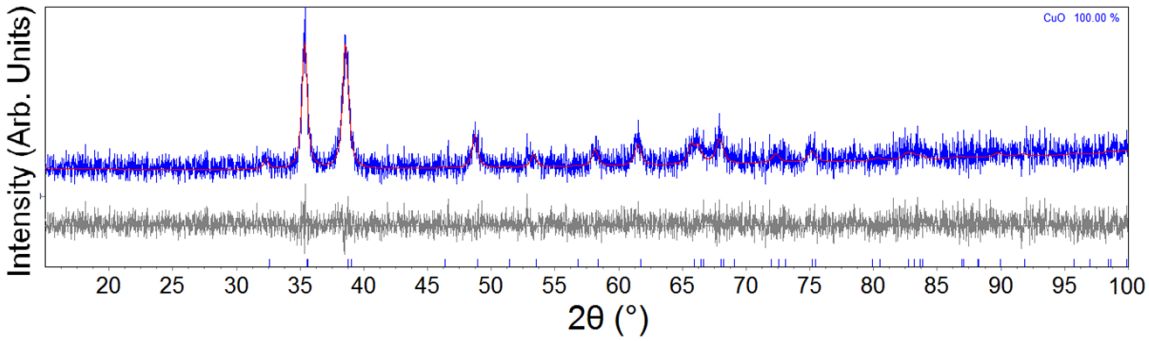

Figure S7: X-ray diffraction data of heat-treated Cu_2O nanostructures after whole powder pattern decomposition fitting.

Table S4: Whole pattern decomposition fitting results for Cu_2O nanostructures after heat treatment at 400 °C for 1 hour.

Phase Name	**CuO (100%)**		
R-Bragg	2.867		
Space group	C1c1		
Cell Volume	80.75(10)		($Å^3$)
Crystallite size (Lvol-IB)	19.3(10)		(nm)
Crystal Linear Absorption Coefficient	286.16(36)		(1/cm)
Crystal Density	6.5429(83)		(g/cm^3)
Lattice Parameters	a	4.6709(32)	(Å)
	b	3.4227(27)	(Å)
	c	5.1190(37)	(Å)
	β	99.338(31)	°

3. Characterisation of electrodeposited metallic Cu

A representative scanning electron microscopy image of the electrodeposited metallic Cu is shown in Figure S8.

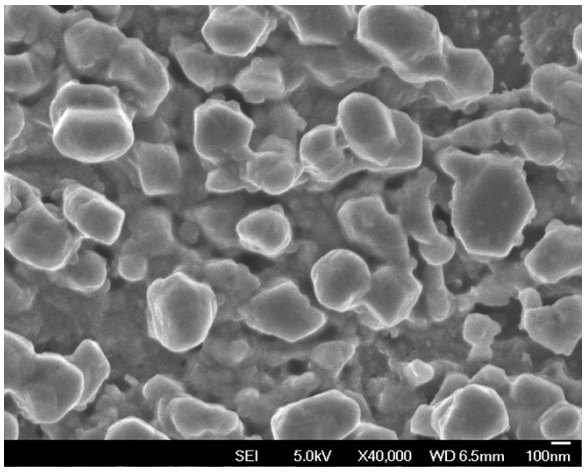

Figure S8: SEM image of electrodeposited Cu

A quantitative analysis of the XRD data of electrodeposited Cu was performed (Figure S9 and Table S5). Reference data for metallic Cu was taken from literature.[5] Only metallic Cu peaks were detected. The blue, red and grey lines represent observed XRD data, calculated pattern from the reference data, and difference plot respectively.

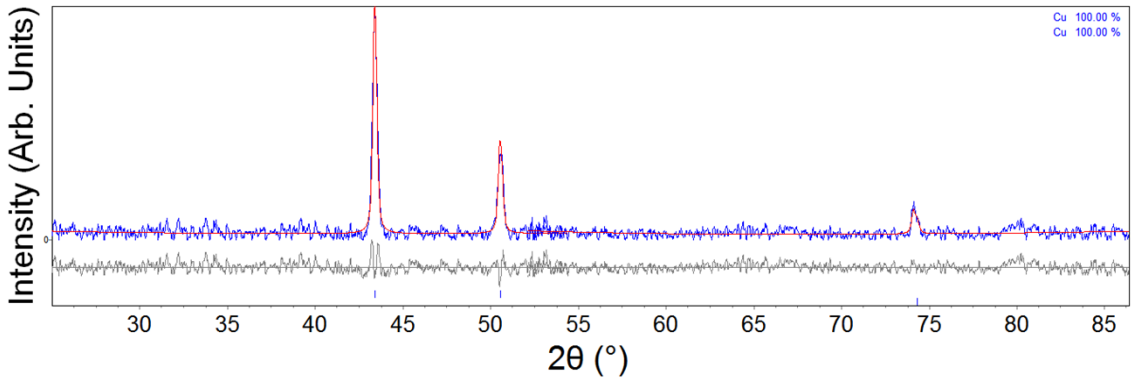

Figure S9: X-ray diffraction data of electrodeposited Cu. The diffraction data was collected with Bruker Discover D8 with GADDS area detector at two different detector positions.

Table S5: Whole pattern decomposition fitting results for electrodeposited Cu.

Phase Name	**Cu (100%)**	
R-Bragg	2.695	
Space group	Fm-3m	
Cell Volume	46.96(9)	($Å^3$)
Crystallite size (Lvol-IB)	76(3)	(nm)
Crystal Linear Absorption Coefficient	466.1(9)	(1/cm)
Crystal Density	8.99(2)	(g/cm^3)
Lattice Parameters	a 3.608(2)	(Å)

4. Online electrochemical mass spectrometry

Online electrochemical mass spectrometry was used to analyse gaseous products liberated from H_2O_2-treated CuO nanostructured films held at 1.75 V. The design of the cell was adapted from the work of Koper et al.[8] The probe was fitted with a porous PTFE membrane (Porex® PM2010, 15-25 µm pore size, 50-60% porosity). It was mounted ~0.5 mm away from the anode in order to minimise the time delay due to mass transfer of O_2. A mass spectrometer (ThermoStar GSD 320 T1, Pfeiffer Vacuum) was used for analysing the gaseous products. Time resolved measurements of oxygen demonstrated significant increase of O_2 after OER was started (mass 32, Figure S10a). Similar conclusion can be drawn by comparing O_2 concentration before and during OER using wide mass survey scan (Figure S10b).

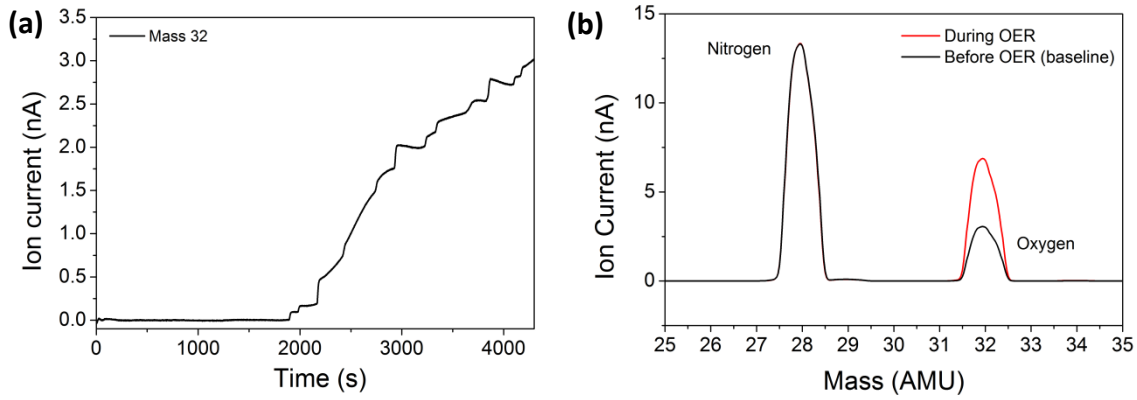

Figure S10: Online mass spectrometry results of H_2O_2-treated CuO nanostructures: (a) time resolved monitoring of oxygen (mass 32) and (b) wide survey scan comparison between nitrogen (mass 28) and oxygen (mass 32) before and during OER.

5. Calculation of turnover frequencies (TOF) of O_2 production

The turnover frequency in this work is defined as the number of O_2 molecules evolved per active site per second. We assume that four electrons are required to form one O_2 molecule, and that all metal atoms present are catalytic- active. Taking the case of CuO, its TOF can be calculated as:

$$TOF_{CuO} = \frac{\left[\frac{i}{4 \cdot e}\right]}{\left[\frac{m_{CuO} \cdot N_A}{MW_{CuO}}\right]} \text{ s}^{-1}$$

where

i is the current (in Ampere);

e is the electric charge carried by a single electron constant ($1.602176565\times10^{-19}$ C);

m_{CuO} is the weight loading of CuO catalyst;

N_A is the Avogadro's constant (6.02214129×10^{23} mol^{-1});

MW_{CuO} is the molecular weight of CuO catalyst (79.545 g mol^{-1}).

Sample calculations: Taking H_2O_2-treated CuO nanostructures as an example. The measured current at 1.75 V vs. RHE (taken from Figure 2b at 2200 s) is 2.508×10^{-4} A.

The total number of oxygen evolution reactions that have occurred per second, assuming 4 electrons are transferred for each reaction is $\frac{2.508\times10^{-4}\,A}{4\times1.602\times10^{-19}\,C}$ = 3.914×10^{14} s^{-1}

The weight loading of CuO catalyst is 1.786×10^{-5} g.

The number of Cu sites in the H_2O_2-treated CuO nanostructures is

$$\frac{1.786\times10^{-5}\,g\times6.022\times10^{23}\,mol^{-1}}{79.545\,g\cdot mol^{-1}} = 1.352\times10^{17}$$

Assuming that the all Cu atoms participated in the OER, the TOF is therefore $\frac{3.914\times10^{14}}{1.352\times10^{17}}$ = 2.895×10^{-3} s^{-1}.

The TOFs for Cu and Cu_2O catalysts can be similarly calculated. The TOF values calculated for all catalysts used in this work are compared with the values found or calculated from the literature (Table S6).

Table S6: TOF values of various catalysts in the literature and in this work. CA: chronoamperometry, LSV: linear sweep voltammetry.

Ref.	Catalyst	Current (A)	TOF (s^{-1})	Note	Current (A)	TOF (s^{-1})	Note
This work	H_2O_2 -treated CuO nanostructures	2.51×10^{-4}	2.90×10^{-3}	Fig 2b and Fig 2d, η=520 mV	2.85×10^{-5}	3.30×10^{-4}	Fig 2a, η = 400 mV
		2.44×10^{-4}	2.82×10^{-3}		2.72×10^{-5}	3.14×10^{-4}	Fig S12, η = 400 mV
		2.05×10^{-4}	2.37×10^{-3}		2.35×10^{-5}	2.71×10^{-4}	Fig S12, η = 400 mV
This work	Cu_2O nanostructures (precursor)	5.81×10^{-5}	6.02×10^{-4}	Fig 2b and Fig 2d, η=520 mV	9.55×10^{-6}	9.90×10^{-5}	Fig 2a, η = 400 mV
		5.70×10^{-5}	5.91×10^{-4}		9.28×10^{-6}	9.63×10^{-5}	LSV data not shown, η = 400 mV
		4.12×10^{-5}	4.28×10^{-4}		9.35×10^{-6}	9.70×10^{-5}	
This work	Cu_2O (Commercial)	9.01×10^{-6}	9.33×10^{-5}	Fig 2b and Fig 2d, η=520 mV	2.66×10^{-6}	2.80×10^{-5}	Fig 2a, η = 400 mV
		9.93×10^{-6}	1.03×10^{-4}		1.87×10^{-6}	1.94×10^{-5}	LSV data not shown, η = 400 mV
		1.34×10^{-5}	1.39×10^{-4}		1.98×10^{-6}	2.06×10^{-5}	
This work	Electro deposited Cu	1.07×10^{-5}	6.04×10^{-5}	Fig 2b and Fig 2d, η=520 mV	7.27×10^{-7}	4.11×10^{-6}	Fig 2a, η = 400 mV
		7.65×10^{-6}	4.32×10^{-5}		1.63×10^{-6}	9.18×10^{-6}	LSV data not shown, η = 400 mV
		7.52×10^{-6}	4.25×10^{-5}		1.99×10^{-6}	1.12×10^{-5}	
Kumar et al.[9]	Cu/Glassy carbon	1.9×10^{-5}	2.8×10^{-5}	Fig 13a. BET surface area, η=520 mV	7.2×10^{-6}	1.1×10^{-5}	Fig 13a. BET surface area, η = 400 mV
Kumar et al.[10]	Cu_2O/Glassy carbon	1.8×10^{-4}	5.0×10^{-5}	Fig 8, η=520 mV	1.1×10^{-4}	3.1×10^{-5}	Fig 8, η = 400 mV
Kanan et al.[11]	Co Pi	$\sim8\times10^{-4}$	N.A.	Fig. 1b, η=473 mV	N.A.	$\geq7\times10^{-4}$	Obtained from Jiao & Frei[12], η = 410 mV
Rasiyah et al.[13]	Co_3O_4	N.A.	N.A.	N.A.	N.A.	$\geq8\times10^{-4}$	Obtained from Jiao & Frei[12], η = 414 mV
Iwakura et al.[14]	Co/Co_3O_4	N.A.	N.A.	N.A.	5.1×10^{-3}	5.5×10^{-4}	Fig 3, η = 400 mV
Fekete et al.[15]	β-MnO_2 nano	3.9×10^{-3}	9.0×10^{-4}	Fig 6b. Estimated loading 0.986 mg, η = 520 mV	1.8×10^{-3}	4.2×10^{-4}	Fig 6b. Estimated loading 0.986 mg, η = 400 mV
Kim et al.[16]	$CaMn_2O_5$/C	9.8×10^{-5}	5.8×10^{-4}	Fig S3a. Scan 9. Loading 0.05mg, η = 520 mV	3.9×10^{-5}	2.3×10^{-4}	Fig S3a. Scan 9. Loading 0.05mg, η = 400 mV

6. H_2O_2 treatment of Cu disc electrodes.

The H_2O_2 treatment can also be used to enhance the OER activity of pristine Cu discs (10 mm diameter, Fig S11). The H_2O_2-treated Cu discs also exhibited a more stable O_2–evolving catalytic activity.

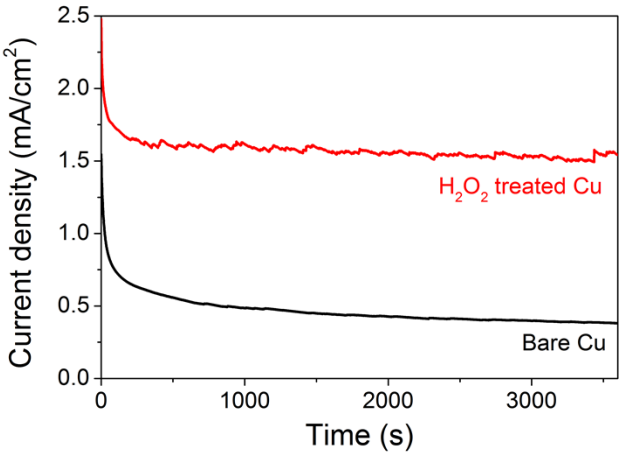

Figure S11: Chronoamperomograms of bare 10 mm Cu disc before (black trace) and after five cycles of H_2O_2 treatments (red trace). Potential applied: 1.75 V. Electrolyte: 0.1 M KOH.

7. Surface area of catalysts

The surface areas of the electrodes were determined by both the double layer capacitance method and Brunauer–Emmett–Teller (BET) method.

Double layer capacitance method: Cyclic voltammetry curves of the electrodes were recorded at scan rates between 0.02 and 0.3 V s^{-1}. The capacitative current density was plotted as a function of scan rate, which gave a linear plot. C_{dl} values of 28 and 60 µF cm^{-2} were respectively used for an ideally smooth metal surface and an oxide surface.[17-19] The slope of the plot/C_{dl} µF cm^{-2} gives the roughness factor (R_F) of the surface. The electrochemically determined surface area is then given by R_F × geometric surface area (0.0707 cm^2). The calculated values are summarised in Table S7.

Brunauer–Emmett–Teller (BET) method: The surface areas of the powder samples were measured on a Micromeritics ASAP 2020 at 77 K. The samples were degassed at 460 K prior to N_2 sorption. The measured values are summarised in Table S7.

Table S7: Tabulation of surface areas determined by the double layer capacitance method and BET method.

Catalyst	Capacitance (mF/cm^2)	Surface roughness factor (R_F)	EC-determined surface area (cm^2)	BET data (m^2/g)	BET surface area (cm^2)	BJH Ads average pore diameter (nm)
Commercial Cu_2O	0.076	1.26	0.09	6.06	1.08	12.65
Cu_2O nanostructures (untreated)	0.073	1.21	0.09	6.19	1.1	8.43
H_2O_2-treated CuO nanostructures	0.094	1.56	0.11	17.63	3.16	32.82
Electrodeposited Cu	0.087	3.10	0.22	-	-	-
Heat treated CuO nanostructures	0.065	1.08	0.08	5.20	0.93	37.60

Considering the data given by both methods, the surface areas of the Cu catalysts varied within a factor of 3. Note that the electrochemical determined surface areas are smaller than that of the BET determined surface areas. This can be attributed to the lower electrochemical accessibility of the metal or metal oxide sites due to obstruction by the Nafion binder.[20]

8. Linear scanning voltammetry of H_2O_2-treated CuO nanostructures

The stability of H_2O_2-treated CuO nanostructures was also assessed by consecutive linear scanning voltammetry scans from 1 to 1.75 V (Fig S12). The H_2O_2-treated CuO nanostructures were stable under the test conditions, which took about 2 hours.

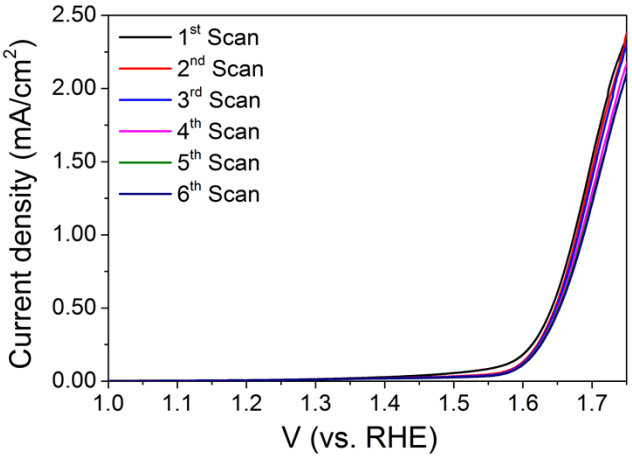

Figure S12: Multiple LSV curves of H_2O_2-treated CuO nanostructures. The six consecutive LSV scans were performed over ~2 hours. Scan rate: 1 mV/s. Electrolyte: 0.1 M KOH.

9. Raman data and Raman peak assignments.

The Raman spectra of the Cu_2O nanostructure precursors and H_2O_2-treated CuO nanostructures were measured and presented in Figure S13a. Peaks corresponding to Cu_2O and CuO were observed (Table S8 and S9).

CuO films formed by the anodic oxidation of a Cu substrate in KOH electrolyte were also studied.[21] No other inorganic or organic reagents were used in the synthesis. The transient Raman peak at 603 cm^{-1} was also observed on this CuO film (Figure S13b). This eliminates the possibility that the Raman vibration at 603 cm^{-1} originates from reagents used in the synthesis of the CuO nanostructures.

The Raman peaks observed in this work are compared with previous values, and summarised in Tables S8 and S9.

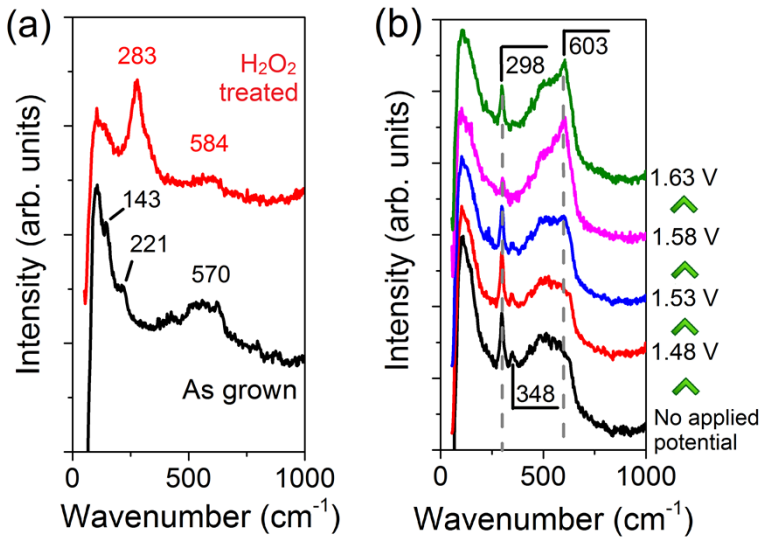

Figure S13: (a) Raman spectra (taken in air) of the Cu_2O precursor and H_2O_2-treated CuO nanostructures; (b) In-situ Raman spectra of CuO grown by electro-oxidation of Cu metal in KOH.

Table S8: Raman frequencies of Cu_2O. §: this work.

Sample	Frequencies (cm^{-1})				
Cu_2O nanostructures without applied potential and at 1.48V, Fig. 3c§	143	221		540	620
Cu_2O nanostructures (measured in air), Fig. S13a§	143	221		570	
Anodically-formed Cu_2O film[22]	145	214			644
Electrodeposited Cu film on Pt disc[22]	150	222	528	581	623

Table S9: Raman frequencies of CuO. §: this work.

Sample	Frequencies (cm^{-1})			
H_2O_2-treated CuO nanostructures without applied potential and at 1.48-1.53 V, Fig 3a§		298	343	612
H_2O_2-treated CuO nanostructures (measured in air), Fig. S13a§		283		584-592
CuO nanobelt powders[23]		282	337	613
CuO nanocrystals[24]		288-295	330-342	621-628
CuO electrodeposited on Cu disc[25]	250	300	347	635

10. Synthesis and characterisation of Cu^{III}-containing $NaCuO_2$

$NaCuO_2$ was synthesised according to the procedure reported by Ono et al.[26]. The XRD and whole powder decomposition fitting data are presented respectively in Fig S14 and Table S10. The reference crystallographic data of $NaCuO_2$ was taken from the literature.[27] The blue, red and grey lines represent observed XRD data, calculated pattern from the reference data, and difference plot respectively. $NaCuO_2$ is observed together with small amounts of CuO.

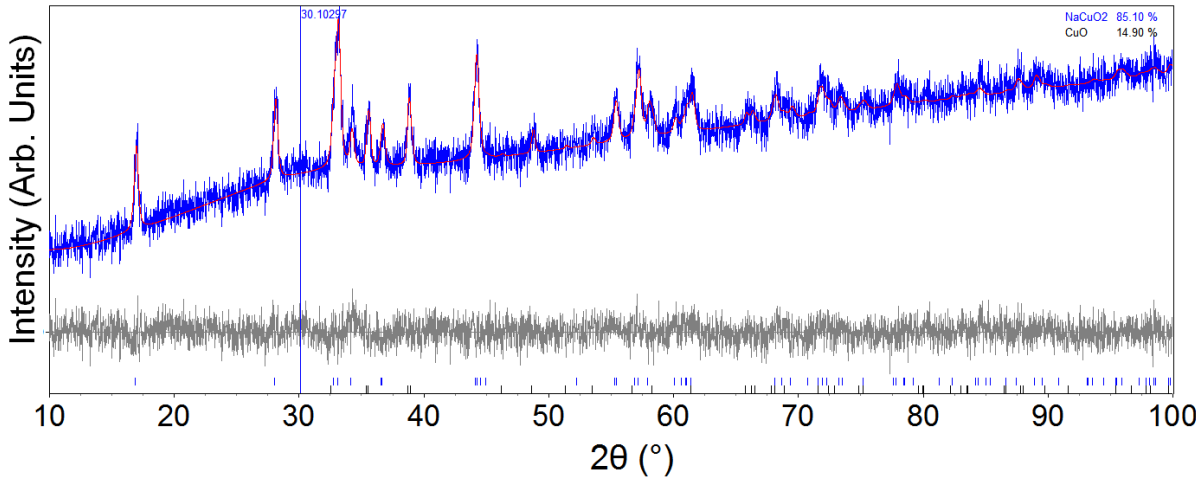

Figure S14: X-ray diffraction data of $NaCuO_2$ after whole powder pattern decomposition fitting.

Table S10: Whole pattern decomposition fitting results for $NaCuO_2$ and CuO powder mixture.

Phase 1 Name	**$NaCuO_2$ 85.0(5) %**		
R-Bragg	2.708		
Space group	C2/m		
Cell Volume	91.888(48)		($Å^3$)
Crystallite size (LVol-IB)	20.49(56)		(nm)
Crystal Linear Absorption Coefficient	136.218(72)		(1/cm)
Crystal Density	3.8800(20)		(g/cm^3)
Lattice Parameters	a	6.3614(18)	(Å)
	b	2.75231(73)	(Å)
	c	6.1091(20)	(Å)
	β	120.787(14)	°
Phase 2 Name	**CuO 15.0(5) %**		
R-Bragg	1.622		
Space group	C1c1		
Cell Volume	81.477(86)		($Å^3$)
Crystallite size (LVol-IB)	28.1(26)		(nm)

Crystal Linear Absorption Coefficient	283.62(30)		(1/cm)
Crystal Density	6.4847(68)		(g/cm^3)
Lattice Parameters	a	4.6884(28)	(Å)
	b	3.4258(20)	(Å)
	c	5.1443(32)	(Å)
	β	99.569(36)	°

The Raman spectrum of the as-synthesized $NaCuO_2$ powder exhibited a very strong peak at 603 cm^{-1} (Fig S15, black trace). As CuO does not have any Raman peak at 603 cm^{-1} (Table S9), this peak must belong to $NaCuO_2$. This assignment was further confirmed by the disappearance of the 603 cm^{-1} peak when the $NaCuO_2$ powder was mixed with water (Fig S15, red trace; only the CuO peak was observed at 276 cm^{-1}).

The occurrence of the 603 cm^{-1} peak from $NaCu^{III}O_2$ supports our assignment of the Raman peak observed on H_2O_2-treated CuO nanostructures at ≥1.58 V to Cu^{III} oxide species (Fig 3a and Fig S15, blue trace).

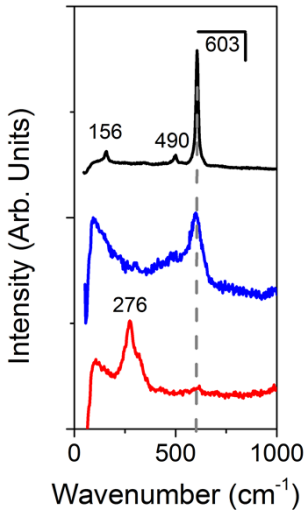

Figure S15: Raman spectrum of as-synthesised $NaCuO_2$ (black trace) showing strong Raman peak at 603 cm^{-1}. This coincides with the observed 603 cm^{-1} peak on H_2O_2-treated CuO nanostructures held at 1.63 V (blue trace). The peak at 603 cm^{-1} seen on $NaCuO_2$ disappeared when water was added to it (red trace).

References cited in the supporting information:

1. G. Pawley, *J. Appl. Crystallogr.*, 1981, **14**, 357-361.
2. H. Toraya, *Rigaku J.*, 1989, **6**, 28-34.
3. A. Kirfel and K. Eichhorn, *Acta Crystallogr. A*, 1990, **46**, 271-284.
4. S. Asbrink and A. Waskowska, *J. Phys.: Condens. Matter*, 1991, **3**, 8173.
5. M. E. Straumanis and L. S. Yu, *Acta Crystallogr. A*, 1969, **25**, 676-682.
6. J. F. Moulder and J. Chastain, *Handbook of X-ray Photoelectron Spectroscopy: A Reference Book of Standard Spectra for Identification and Interpretation of XPS Data*, Physical Electronics Division, Perkin-Elmer Corporation, 1992.
7. M. C. Biesinger, L. W. M. Lau, A. R. Gerson and R. S. C. Smart, *Appl. Surf. Sci.*, 2010, **257**, 887-898.
8. A. H. Wonders, T. H. M. Housmans, V. Rosca and M. T. M. Koper, *J. Appl. Electrochem.*, 2006, **36**, 1215-1221.
9. B. Kumar, S. Saha, M. Basu and A. K. Ganguli, *J. Mater. Chem. A*, 2013, **1**, 4728-4735.
10. B. Kumar, S. Saha, A. Ganguly and A. K. Ganguli, *RSC Adv.*, 2014, **4**, 12043-12049.
11. M. W. Kanan and D. G. Nocera, *Science*, 2008, **321**, 1072-1075.
12. F. Jiao and H. Frei, *Angew. Chem. Int. Ed.*, 2009, **48**, 1841-1844.
13. P. Rasiyah and A. C. C. Tseung, *J. Electrochem. Soc.*, 1983, **130**, 365-368.
14. C. Iwakura, A. Honji and H. Tamura, *Electrochim. Acta*, 1981, **26**, 1319-1326.
15. M. Fekete, R. K. Hocking, S. L. Y. Chang, C. Italiano, A. F. Patti, F. Arena and L. Spiccia, *Energy Environ. Sci.*, 2013, **6**, 2222-2232.
16. J. Kim, X. Yin, K.-C. Tsao, S. Fang and H. Yang, *J. Am. Chem. Soc.*, 2014, **136**, 14646-14649.
17. S. Trasatti and O. A. Petrii, *J. Electroanal. Chem.*, 1992, **327**, 353-376.
18. S. Levine and A. L. Smith, *Discuss. Faraday Soc.*, 1971, **52**, 290-301.
19. J. O. Bockris and T. Otagawa, *J. Phys. Chem.*, 1983, **87**, 2960-2971.
20. P. Staiti, M. Minutoli and F. Lufrano, *Electrochim. Acta*, 2002, **47**, 2795-2800.
21. G. M. Brisard, J. D. Rudnicki, F. McLarnon and E. J. Cairns, *Electrochim. Acta*, 1995, **40**, 859-865.
22. G. Niaura, *Electrochim. Acta*, 2000, **45**, 3507-3519.
23. W. Wang, Q. Zhou, X. Fei, Y. He, P. Zhang, G. Zhang, L. Peng and W. Xie, *CrystEngComm*, 2010, **12**, 2232-2237.
24. J. F. Xu, W. Ji, Z. X. Shen, W. S. Li, S. H. Tang, X. R. Ye, D. Z. Jia and X. Q. Xin, *J. Raman Spectrosc.*, 1999, **30**, 413-415.
25. J. C. Hamilton, J. C. Farmer and R. J. Anderson, *J. Electrochem. Soc.*, 1986, **133**, 739-745.
26. Y. Ono, Y. Yui, K. Asakura, J. Nakamura, M. Hayashi and K. I. Takahashi, *American Journal of Physical Chemistry*, 2014, **3**, 61-66.
27. N. E. Brese, M. O'Keeffe, R. B. Von Dreele and V. G. Young Jr, *J. Solid State Chem.*, 1989, **83**, 1-7.